

Slow photoelectron velocity-map imaging of cold tert-butyl peroxide

Jessalyn A. DeVine, Marissa L. Weichman, Mark C. Babin, and Daniel M. Neumark

Citation: *The Journal of Chemical Physics* **147**, 013915 (2017); doi: 10.1063/1.4979951

View online: <http://dx.doi.org/10.1063/1.4979951>

View Table of Contents: <http://aip.scitation.org/toc/jcp/147/1>

Published by the [American Institute of Physics](#)

COMPLETELY

REDESIGNED!



**PHYSICS
TODAY**

Physics Today Buyer's Guide
Search with a purpose.

Slow photoelectron velocity-map imaging of cold *tert*-butyl peroxide

 Jessalyn A. DeVine,¹ Marissa L. Weichman,¹ Mark C. Babin,¹ and Daniel M. Neumark^{1,2,a)}
¹Department of Chemistry, University of California, Berkeley, California 94720, USA

²Chemical Sciences Division, Lawrence Berkeley National Laboratory, Berkeley, California 94720, USA

(Received 22 February 2017; accepted 28 March 2017; published online 12 April 2017)

Photoelectron spectra of cryogenically cooled \tilde{X}^1A' *tert*-butyl peroxide anions are obtained using slow electron velocity-map imaging. The spectra show highly structured bands corresponding to detachment to the \tilde{X}^2A'' and \tilde{A}^2A' electronic states of the neutral radical and represent a notable improvement in resolution over previous photoelectron spectra. We report an electron affinity of 1.1962(20) eV and a term energy $T_0(\tilde{A}^2A')$ of 0.9602(24) eV for the *tert*-butyl peroxy radical. New vibrational structure is resolved, providing several frequencies for both neutral states. Additionally, the threshold behavior of the photodetachment cross section is investigated within the context of Dyson orbital calculations. *Published by AIP Publishing.* [<http://dx.doi.org/10.1063/1.4979951>]

I. INTRODUCTION

Alkyl peroxy radicals (ROO) are important intermediates in atmospheric oxidation and combustion of organic compounds.^{1–5} Atmospheric reactions of alkyl peroxy radicals with NO result in the formation of tropospheric ozone,^{6,7} motivating a large body of work studying the kinetics of reactions of alkyl peroxy radicals with nitroxides.^{8–10} In the absence of nitroxide pollutants, alkyl peroxy radicals can undergo self-reactions,^{11–13} addition to other species,¹⁴ and unimolecular decomposition.^{15,16} Many of these processes also play a role in low-temperature combustion of hydrocarbons, where alkyl peroxy radicals are an important class of reactive intermediates that exhibit complex, temperature-dependent chemistry.^{17–19} The chemistry of alkyl peroxy radicals has motivated the experimental characterization of their energetics and molecular properties using infrared and electronic spectroscopy,^{20–23} photoionization,²⁴ and negative ion photoelectron spectroscopy.^{25–27} These species have also been investigated in electronic structure calculations.^{28–32} Here, we present slow photoelectron velocity-map imaging (SEVI) spectra of cryogenically cooled *tert*-butyl peroxide (tBuOO[−]) anions, yielding vibrational frequencies as well as the energies of the two lowest electronic states of the neutral *tert*-butyl peroxy radical (tBuOO).

Spectroscopic characterization of the tBuOO radical has been carried out via infrared (IR) absorption in the gas phase and in cryogenic rare gas matrices, yielding several vibrational frequencies ranging from ~300 to 2000 cm^{−1}.^{33,34} Comparison of the frequency shifts upon isotopic substitution permitted vibrational assignments. More recently, near-IR cavity ringdown spectroscopy was used to obtain the vibrationally resolved spectra of the $\tilde{A}^2A' \leftarrow \tilde{X}^2A''$ electronic transition, giving a term energy of 0.9618(19) eV for the \tilde{A}^2A' state of tBuOO as well as C–O–O bending and O–O stretching frequencies for this state.³⁵

The vibrational and electronic structure of the tBuOO radical can also be characterized by negative ion photoelectron spectroscopy of the corresponding anion. This approach has been used previously by Clifford and co-workers²⁶ to obtain the photoelectron spectrum of the closed-shell \tilde{X}^1A' tBuOO[−] anion, probing the \tilde{X}^2A'' and \tilde{A}^2A' electronic states of the neutral radical. These spectra gave an electron affinity (EA) of 1.196(11) eV for \tilde{X}^2A'' tBuOO and the term energy of the excited state. Vibrational frequencies for both electronic states consistent with previous IR experiments were obtained, in addition to frequencies below 300 cm^{−1} that were not previously reported.

Slow photoelectron velocity-map imaging (SEVI) is a variation of traditional photoelectron spectroscopy that uses a tunable detachment laser and a velocity-map imaging (VMI) detection scheme optimized for the detection of slow electrons to obtain photoelectron kinetic energy spectra with sub-meV resolution.³⁶ The resolution of this method is enhanced considerably by cryogenically cooling the anions prior to detachment (cryo-SEVI), resulting in narrower molecular rotational profiles and removal of spectral congestion arising from hot bands. In the current work, we report the cryo-SEVI spectra of the tBuOO system and obtain vibrational resolution for the $\tilde{X}^2A'' \leftarrow \tilde{X}^1A'$ and $\tilde{A}^2A' \leftarrow \tilde{X}^1A'$ electronic bands. The presented spectra show an improvement in resolution over previous results, resolving new vibrational structure and refining previously observed peaks. The attainable resolution in this particular system is ultimately limited by the threshold behavior of the detachment cross section,³⁷ and this is discussed in the context of Dyson orbital calculations.

II. EXPERIMENTAL METHODS

The cryo-SEVI method and apparatus have previously been described in detail.^{36,38,39} In summary, cryogenically cooled anions are mass selected and focused into the interaction region of a VMI electrostatic lens, where they are photodetached and the electron kinetic energy (eKE) distribution is measured. By using a tunable detachment laser and relatively

^{a)} Author to whom correspondence should be addressed. Electronic mail: dneumark@berkeley.edu

low VMI voltages, slow electrons are preferentially detected with high kinetic energy resolution, yielding peaks as narrow as 1.2 cm^{-1} fwhm for detachment from atomic anions.⁴⁰

The tBuOO^- anions are formed by flowing a precursor gas mixture containing trace *tert*-butyl hydroperoxide (tBuOOH) and NF_3 in He through a pulsed molecular beam valve fitted with a circular filament ionizer.⁴¹ Electrons from the ionizer are injected into the precursor gas, leading to dissociative electron attachment to NF_3 that generates fluoride anions. F^- preferentially deprotonates tBuOOH at the hydroxyl site to form the tBuOO^- anion. Anions pass through a radiofrequency (rf) hexapole ion guide and quadrupole mass filter then are deposited into a cryogenically cooled rf octupole ion trap held at 5 K and filled with a buffer gas mixture of 20% H_2 in He.³⁹ Collisions with the cold buffer gas result in efficient cooling of the anions' internal degrees of freedom, yielding ions with typical internal temperatures of ~ 10 K.^{39,42}

After ~ 40 ms in the trap, ions are extracted into an orthogonal Wiley-McLaren time-of-flight mass spectrometer⁴³ and focused into the interaction region of a VMI electrostatic lens,⁴⁴ where mass-selected ions are detached by a tunable dye laser pumped by either the second or third harmonic output of an Nd:YAG laser. The resultant photoelectron distribution is allowed to expand in a field-free region and is then projected onto a 2D detector consisting of two chevron-stacked microchannel plates coupled to a phosphor screen that is photographed by a CCD camera.⁴⁵ Each image is analyzed for individual electron events, the centroids of which are calculated and binned into a grid that is sufficiently fine to ensure that spectral resolution is not limited by pixel size.⁴⁶ Images are accumulated over many laser shots, and the radial and angular distributions are extracted using the Maximum Entropy Velocity Legendre Reconstruction (MEVELER) method.⁴⁷

The VMI spectrometer is calibrated by obtaining images of well-known detachment transitions of atomic O^- and S^- at several photon energies.^{48,49} This procedure determines the relationship between the radius of a feature in the reconstructed image and the corresponding electron kinetic energy (eKE). Due to the approximately constant resolving power, $\Delta\text{eKE}/\text{eKE}$, of the VMI lens, the best resolution is obtained for low-eKE detachment transitions. As such, a single SEVI spectrum consists of scans taken at several photon energies and plotted as a function of electron binding energy (eBE), given by $\text{eBE} = h\nu - \text{eKE}$. To account for threshold effects on the detachment cross section, the individual high-resolution traces are scaled to match the intensities observed in an overview spectrum taken far above threshold.

The cryo-SEVI method also provides the photoelectron angular distribution (PAD) associated with a particular detachment transition, given by⁵⁰

$$\frac{d\sigma}{d\Omega} = \frac{\sigma_{\text{tot}}}{4\pi} [1 + \beta P_2(\cos \theta)], \quad (1)$$

where σ_{tot} is the total detachment cross section, $P_2(x)$ is the second-order Legendre polynomial, θ is the angle of the outgoing electron velocity vector with respect to the laser polarization axis, and β is the anisotropy parameter, which ranges from -1 (parallel detachment) to $+2$ (perpendicular detachment).

At each eKE, the anisotropy parameter reflects the amplitudes and phases of the orbital angular momentum components (*s*, *p*, *d*, ...) comprising the outgoing photoelectron wavefunction and thus provides insight into the shape and symmetry of the molecular orbital from which detachment occurs.^{51,52}

III. CALCULATIONS

All electronic structure calculations were carried out using version 4.4 of the Q-Chem software package.^{53,54} Optimized geometries, harmonic frequencies, and normal mode displacements for the ground state of tBuOO^- and the two lowest doublet states of tBuOO were determined at the B3LYP/6-311+G* level, which has previously been successful in predicting the SEVI spectra for detachment to neutral radical species.⁵⁵⁻⁵⁷ The maximum-overlap method was employed to treat the excited \tilde{A}^2A' neutral state.⁵⁸ The resultant energies, geometries, and frequencies are summarized in Figure S1 and Tables SI and SII of the [supplementary material](#).

Dyson orbitals for the $\tilde{X}^2A'' \leftarrow \tilde{X}^1A'$ and $\tilde{A}^2A' \leftarrow \tilde{X}^1A'$ detachment transitions were calculated using EOM-IP-CCSD/6-311+G*, and these were used as an input for the ezDyson program.⁵⁹ This software determines the contributions to the outgoing electron wavefunction from spherical waves of angular momentum $\ell \leq 5$ and uses this to calculate the detachment cross section and PAD as functions of eKE.⁶⁰ The resultant anisotropy parameters are shown in Figure S2 of the [supplementary material](#), and the detachment cross sections will be discussed in Section V.

Franck-Condon (FC) simulations for the $\tilde{X}^2A'' \leftarrow \tilde{X}^1A'$ and $\tilde{A}^2A' \leftarrow \tilde{X}^1A'$ electronic bands were carried out using ezSpectrum.⁶¹ The B3LYP/6-311+G* geometries, frequencies, and normal mode displacements were taken as input to calculate the Franck-Condon overlap of the anion and neutral vibrational wavefunctions within the harmonic approximation, with Duschinsky mixing included to account for differences in anion and neutral normal modes. The neutral frequencies were scaled by a factor of 0.964 (0.947) for the ground (excited) neutral state so that the ν_{13} (ν_{14}) fundamental matched experiment, and the origin of the simulated spectrum was shifted to the experimental band origin.

In cases where there were discrepancies between the simulated FC profiles and the experimental spectra, small displacements along various normal modes were applied to the ground and excited state neutral geometries in order to see if these discrepancies could be reduced. For a displacement of magnitude δ along normal mode ν_a , the transformed B3LYP/6-311+G* geometry is given by

$$\vec{r}^{(i)} = \vec{r}_{eq}^{(i)} + \delta \vec{q}_a^{(i)}, \quad (2)$$

where $\vec{r}_{eq}^{(i)}$ and $\vec{r}^{(i)}$ are the equilibrium and shifted positions of the *i*th atom, respectively, and $\vec{q}_a^{(i)}$ is the displacement vector for the *i*th atom associated with mode ν_a . Normal mode displacement vectors used for these adjustments of the neutral geometries are provided in Table SIII of the [supplementary material](#), and further details of these calculations are provided in Section I of the [supplementary material](#).

IV. RESULTS

Figure 1 shows the full cryo-SEVI spectrum of tBuOO^- . In this figure and those that follow, the blue traces are low-resolution overview scans taken at photon energies well above the electronic band of interest, resulting in values of eKE ranging from 2000 to 6000 cm^{-1} for the band origins. Black traces are high-resolution SEVI scans taken near the detachment threshold for various peaks in the spectrum, yielding much slower electrons in the vicinity of these peaks.

Two distinct bands can be seen in Figure 1; expanded views of these two regions are shown in Figure 2 (eBE $< 16\,000\text{ cm}^{-1}$) and Fig. 3 (eBE $> 16\,000\text{ cm}^{-1}$). All features in Figure 1 showed negative anisotropy parameters (Eq. (1)) for the observed kinetic energies, as will be addressed in more detail in Section V. The general structure of the two bands is similar, with both Figures 2 and 3 showing a dominant progression (X1-X4-X12-X18 and A1-A4-A7) modulated by one or more weaker, lower-frequency progressions. Similar structure was also observed by Clifford and co-workers,²⁶ albeit in lower resolution. From the previous photoelectron spectra of this system as well as the calculated energies, the lower-eBE region in Figure 2 is assigned to the $\tilde{X}^2A'' \leftarrow \tilde{X}^1A'$ ground state band, and the higher-eBE region in Figure 3 is assigned to the $\tilde{A}^2A' \leftarrow \tilde{X}^1A'$ excited state band. Peak widths in the ground

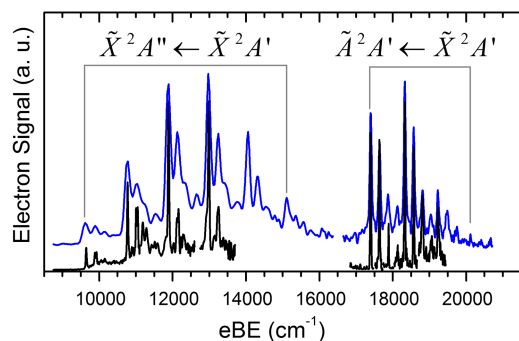


FIG. 1. Cryo-SEVI spectrum of tBuOO^- showing detachment to the \tilde{X}^2A'' and \tilde{A}^2A' electronic states of the neutral radical. The blue traces are low-resolution overview spectra taken far above threshold, and the black traces are lower-eKE, high-resolution SEVI scans scaled to match overview intensities and spliced together.

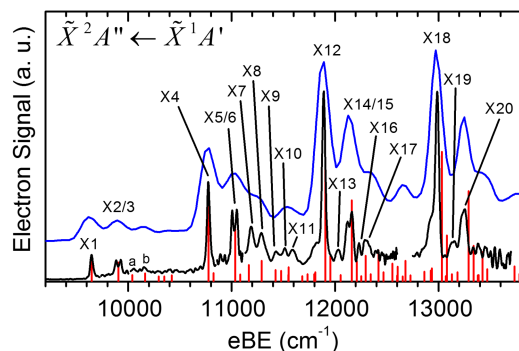


FIG. 2. Cryo-SEVI spectrum of tBuOO^- in the region of the $\tilde{X}^2A'' \leftarrow \tilde{X}^1A'$ electronic band. The blue trace is an overview spectrum taken with a photon energy of $17\,698\text{ cm}^{-1}$, and the black traces are high-resolution scans taken close to threshold. A Franck-Condon calculation based on B3LYP/6-311+G* results is shown as the red stick spectrum.

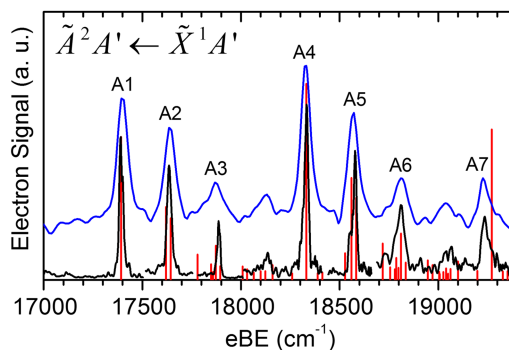


FIG. 3. Cryo-SEVI spectrum of tBuOO^- in the region of the $\tilde{A}^2A' \leftarrow \tilde{X}^1A'$ electronic band. The blue trace is an overview spectrum taken with a photon energy of $20\,814\text{ cm}^{-1}$, and the black traces are high-resolution scans taken close to threshold. A Franck-Condon calculation based on B3LYP/6-311+G* results is shown as the red stick spectrum.

and excited state bands are $\sim 40\text{ cm}^{-1}$ and 20 cm^{-1} , respectively. The peaks are somewhat broader than usually obtained in cryo-SEVI measurements, particularly in the ground state band; this broadening reflects low detachment cross sections near the threshold and is discussed in Section V.

Due to the absence of vibrational hot bands resulting from the low temperature of cryo-SEVI, the first feature in each band (X1 in Figure 2, A1 in Figure 3) corresponds to the vibrational origin (0_0^0) transition to the relevant neutral electronic state, providing useful information on the electronic energetics of the neutral tBuOO radical. The position of peak X1 gives the electron affinity $\text{EA} = 1.1962(20)\text{ eV}$ for the neutral tBuOO radical, which represents an order-of-magnitude improvement

TABLE I. Peak positions, shifts from the origin, and assignments of vibrational features in the $\tilde{X}^2A'' \leftarrow \tilde{X}^1A'$ electronic band of the tBuOO^- cryo-SEVI spectrum. Uncertainties in peak positions correspond to the width parameter of a Gaussian fit to the experimental peak.

Peak	eBE (cm^{-1})	Shift (cm^{-1})	Assn.
X1	9 648 (16)	0	0_0^0
X2	9 884 (14)	236	22_0^1
X3	9 927 (13)	279	21_0^1
a ^a	10 054 (13)	407	19_0^1
b ^a	10 157 (16)	510	21_0^2
X4	10 776 (15)	1129	13_0^1
X5	11 007 (12)	1360	$13_0^1 22_0^1$
X6	11 048 (14)	1401	$13_0^1 21_0^1$
X7	11 189 (25)	1542	$13_0^1 19_0^1$
X8	11 289 (32)	1642	$13_0^1 21_1^1$
X9	11 435 (30)	1788	$13_0^1 19_0^1 21_1^1$
X10	11 512 (21)	1865	$13_0^1 17_0^1$
X11	11 590 (29)	1943	$13_0^1 21_0^3$
X12	11 890 (16)	2243	13_0^2
X13	12 030 (21)	2382	$12_0^1 13_0^1$
X14	12 119 (20)	2472	$13_0^2 22_0^1$
X15	12 164 (15)	2517	$13_0^2 21_0^1$
X16	12 230 (10)	2583	$12_0^1 13_0^1 21_0^1$
X17	12 305 (34)	2657	$13_0^2 19_0^1$
X18	12 986 (17)	3339	13_0^3
X19	13 145 (42)	3498	$12_0^1 13_0^2$
X20	13 243 (76)	3596	$13_0^3 21_0^1$

^aThese features are visible in the overview spectrum but are very close to the S/N level in the higher-resolution scans.

TABLE II. Peak positions, shifts from the origin, and assignments of vibrational features in the $\tilde{A}^2A' \leftarrow \tilde{X}^1A'$ electronic band of the tBuOO⁻ cryo-SEVI spectrum. Uncertainties in peak positions correspond to the width parameter of a Gaussian fit to the experimental peak.

Peak	eBE (cm ⁻¹)	Shift (cm ⁻¹)	Assn.
A1	17 392 (10)	0	0 ₀ ⁰
A2	17 636 (11)	244	x ₀ ¹
A3	17 888 (7)	495	x ₀ ²
A4	18 331 (10)	939	14 ₀ ¹
A5	18 577 (11)	1184	14 ₀ ¹ x ₀ ¹
A6	18 807 (23)	1415	14 ₀ ¹ x ₀ ²
A7	19 238 (19)	1846	14 ₀ ²

in resolution over previous results.²⁶ The position of peak A1 relative to X1 provides the term energy of $T_0(\tilde{A}^2A')$ = 0.9602(24) eV for the first neutral excited state, well within the error of the term energy measured using near-IR cavity ringdown spectroscopy.³⁵

FC simulations for both electronic bands are shown as red stick spectra in Figures 2 and 3 and can be seen to provide good agreement with the observed structure. This agreement facilitates assignment of several vibrational features, summarized in Tables I and II for the ground and excited states, respectively. The calculated normal coordinates for active modes participating in the spectra are shown in Figure 4. Two peaks assigned in Table I, a and b, are visible in the ground state band overview and line up quite well with simulated features but are just barely above the S/N level in the higher resolution traces.

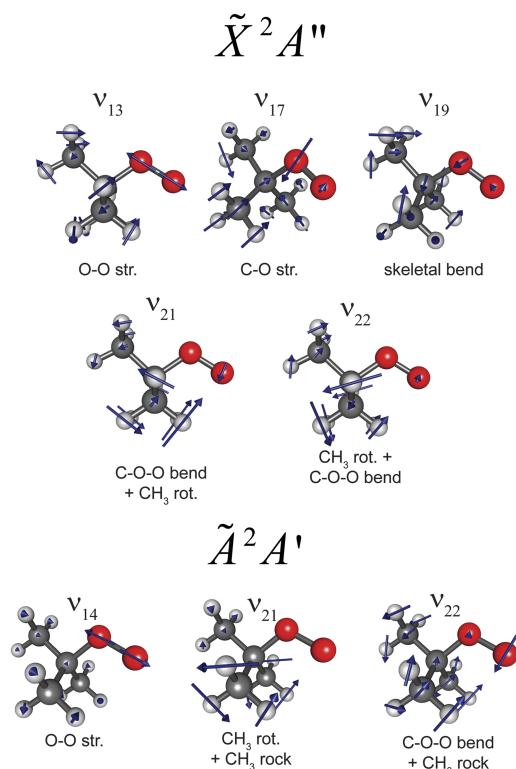


FIG. 4. Franck-Condon active vibrational modes of the \tilde{X}^2A'' (top) and \tilde{A}^2A' (bottom) electronic states of neutral tBuOO observed in the cryo-SEVI spectra. Brief descriptions of the molecular motions are included for clarity.

V. DISCUSSION

A. Spectral assignments

Term values and vibrational frequencies extracted from the present results are summarized in Table III and compared to available literature data. Vibrational frequencies were determined by measuring peak displacements from the appropriate band origin. Error bars were obtained using standard error propagation formulas, taking the uncertainty in peak positions to be the width parameter obtained from a Gaussian fit to the experimental peak and taking the covariance between peak positions to be zero. Anharmonicity is expected to be non-negligible for the dominant progression in both electronic bands given the visible decrease in peak spacing in the main X1-X4-X12-X18 and A1-A4-A7 progressions.

The previously reported photoelectron spectrum²⁶ found $\nu_{13} = 1130(90)$ and $\nu_{21} = 245(90)$ cm⁻¹ for the FC-active ground state O–O stretching and C–O–O bending modes, respectively. Two frequencies were reported but not assigned for the excited state band: $\nu_r = 930(90)$ and $\nu_s = 240(90)$ cm⁻¹. In the present spectra, comparison to the FC simulations confirms the previous assignment of the ν_{13} progression in the ground state band and enables the assignment of the excited state ν_r progression as a similar O–O stretching mode (ν_{14} , Figure 4). The experimental O–O stretching frequencies are found to be $\nu_{13} = 1129(20)$ and $\nu_{14} = 939(14)$ cm⁻¹ for the ground and excited states, respectively, in agreement with O–O stretching frequencies observed in infrared experiments.^{34,35}

The assignment of the lower-frequency progressions is slightly more challenging. Figure 2 demonstrates that peaks in the ground state band associated with the low-frequency ν_{21} mode reported in the previous work are closely spaced doublets with a ~ 40 cm⁻¹ splitting (peaks X2/3 and X5/6), whereas there is only a single peak in the simulations. In addition, several smaller peaks are seen and assigned to excitation of additional lower frequency modes, as indicated in Tables I and III.

The simulated peak for the two doublets involves ν_{21} , which is best described as CH₃ internal rotations with some C–O–O bending character (Figure 4). The C–O–O bending character results in a larger frequency than is typically expected for internal rotations. The other doublet component is likely

TABLE III. Experimental and calculated molecular properties of the neutral tBuOO radical obtained in the present work, as well as comparison to available literature values. Reported vibrational frequencies correspond to the energy of the fundamental ($n = 1$) level relative to the neutral zero-point energy.

State	Parameter	Expt.	Calc.	Lit.
\tilde{X}^2A''	EA, eV	1.1962 (20)	1.0274	1.196 (6) ²⁶
	ν_{22} , cm ⁻¹	236 (21)	265	245 (90) ²⁶
	ν_{21} , cm ⁻¹	279 (21)	267	
	ν_{19} , cm ⁻¹	410 (29)	406	403 (3) ³⁴
	ν_{17} , cm ⁻¹	740 (26)	728	730 (2) ³⁴
	ν_{13} , cm ⁻¹	1129 (22)	1171	1124 (2) ³⁴
	ν_{12} , cm ⁻¹	1254 (26)	1221	
\tilde{A}^2A'	T_0 , eV	0.9602 (24)	0.9836	0.9618 (19) ³⁵
	ν_x , cm ⁻¹	244 (15)	241/265	240 (90) ²⁶
	ν_{14} , cm ⁻¹	939 (14)	992	938 (2) ³⁵

due to vibrational mode ν_{22} , which corresponds to a similar totally symmetric motion as ν_{21} (though with less C–O–O bending character), and is calculated to be only 2 cm^{-1} lower in frequency. A reasonable explanation for the observed splitting is that both vibrational modes are in fact FC-active, and the activity of ν_{22} is not captured in the FC simulations shown in Fig. 2 due to slight inaccuracies in the B3LYP/6-311+G* optimized geometries resulting from treatment of the methyl groups.

To quantify the geometry displacement necessary to yield Franck-Condon activity in the ν_{22} mode, displacements along this normal coordinate as defined in Eq. (3) were applied to the calculated \tilde{X}^2A'' neutral geometry, and the resultant geometries were used to generate the FC simulations shown in Figure S3 of the [supplementary material](#). We find that displacements of magnitude $0.3 < \delta < 0.4$ along ν_{22} are sufficient to yield a doublet of peaks with approximately equal intensities. This geometry displacement, described more quantitatively in Table SIV of the [supplementary material](#), corresponds to a slight rotation of the out-of-plane methyl groups as well as a $<2^\circ$ increase in the C–O–O bond angle. Thus, the lower-frequency progression in the ground state band that was resolved in the previous photoelectron spectrum is actually a progression in two close-lying vibrational modes, with frequencies $\nu_{21} = 279(21)$ and $\nu_{22} = 236(21)\text{ cm}^{-1}$.

In the excited state band, the FC simulation predicts that two features with similar intensity should be present where peak A2 appears, but only one feature is observed. Although the simulated peaks involving single excitation of the ν_{22} and ν_{23} modes are 25 cm^{-1} apart, the experimental peak A2 is only 20 cm^{-1} wide (i.e., the same width as the band origin, A1), suggesting that most of its intensity comes from a single transition. Again, we attribute this discrepancy to the high sensitivity of the FC intensities to the geometries and normal modes used to calculate them.

Comparison to the simulated spectra indicates that peak A2 corresponds to either the ν_{21} or ν_{22} fundamental. As such, small displacements along these normal modes were carried out on the excited state geometry, and the resultant FC simulations are shown in Figures S4 and S5 of the [supplementary material](#). A displacement of magnitude $0.2 < \delta < 0.3$ along ν_{21} results in the disappearance of this mode from the simulated spectra and corresponds to a similar geometry displacement as for the ground state band, whereas a displacement of magnitude $0.1 < \delta < 0.2$ along ν_{22} is required for peak A2 to correspond to the ν_{21} fundamental. The displacement along the ν_{22} mode results in a slight rotation of the methyl groups, as well as a 3.2° decrease in the C–O–O bond angle. As can be seen from Figures S4 and S5 in the [supplementary material](#), elimination of either ν_{21} or ν_{22} from the spectrum results in similar agreement with the experimental results, preventing definitive assignment of the single-component low-frequency excited state progression. We thus refer to this unassigned frequency as ν_x , and this notation is used in Tables II and III to emphasize that this frequency may correspond to either ν_{21} or ν_{22} .

The FC-activity of O–O stretching modes can be understood from the localized nature of the detached anion orbitals. As can be seen in Figure 5, the Dyson orbitals for

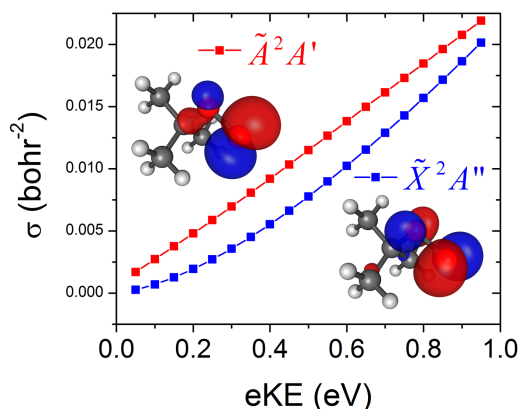


FIG. 5. Calculated detachment cross sections for the $\tilde{X}^2A'' \leftarrow \tilde{X}^1A'$ (blue) and $\tilde{A}^2A' \leftarrow \tilde{X}^1A'$ (red) electronic bands based on Dyson orbital calculations of $t\text{BuOO}^-$. The Dyson orbitals for both detachment transitions are also shown and are labeled with the corresponding neutral state.

detachment to both the \tilde{X}^2A'' and \tilde{A}^2A' neutral states appear to be antibonding orbitals localized on the O–O bond. Detachment to both of these states removes density from these orbitals, resulting in a decrease in the length of this bond. This geometry difference between anion and neutral provides FC activity to ν_{13} in the ground state band and ν_{14} in the excited state band. Similarly, the involvement of modes possessing some CH_3 rotation character in the ground state band is likely due to the removal of electron density that can interact with the out-of-plane methyl groups. For the excited state, the lower-frequency progression corresponds to a C–O–O bending mode (ν_{22}), due to the removal of electron density within the symmetry plane upon detachment. The similar character of the two Dyson orbitals is likely the cause for the relatively small term energy of the \tilde{A}^2A' neutral state of $t\text{BuOO}$, which is similar to those observed for the first excited states of other simple ROO radicals.^{27,35}

B. Detachment cross sections

While the resolution of the photoelectron spectra presented here is improved compared to previous work on this system, the ultimate peak widths obtained are not as narrow as is often seen in cryo-SEVI experiments, particularly for the \tilde{X} band. This highlights the effects of the Wigner threshold law³⁷ on our ability to obtain a high-resolution cryo-SEVI spectrum, which in turn hinges on our ability to obtain SEVI spectra at low eKE. The Wigner threshold law states that the photodetachment cross section σ near the threshold for a particular transition scales as

$$\sigma \propto (\text{eKE})^{\ell+1/2}, \quad (3)$$

where ℓ is the orbital angular momentum of the outgoing electron. Therefore, detachment transitions resulting in photoelectrons with appreciable s -wave ($\ell = 0$) character can be observed at photon energies close to the threshold, yielding low kinetic energies and the highest possible resolution. For photodetachment transitions dominated by higher values of ℓ , the cross section drops more rapidly as the photon energy approaches the photodetachment threshold, essentially raising the minimum eKE at which there is sufficient SEVI signal to

observe a particular transition and leading to decreased energy resolution.⁵⁵

The factors determining which values of ℓ contribute to photodetachment have been discussed elsewhere⁵¹ and can be quantitatively assessed for a particular system by performing a Dyson orbital analysis in which the photodetachment cross section is calculated as a function of eKE .^{59,60} The results for photodetachment of $tBuOO^-$ to the \tilde{X} and \tilde{A} states are shown in Figure 5. Both cross sections decrease more rapidly than $(eKE)^{1/2}$, indicating that partial waves with $\ell > 0$ contribute significantly to near-threshold photodetachment. This is confirmed by a partial wave decomposition analysis of the photoelectron wavefunctions for high- eKE s obtained in the Dyson orbital calculation, details of which are provided in Section II of the [supplementary material](#). As can be seen from Table SV of the [supplementary material](#), this analysis reveals that for an eKE of 1.05 eV, detachment to the \tilde{X}^2A'' neutral state results in photoelectrons with larger contributions from $\ell > 0$ spherical waves than detachment to the \tilde{A}^2A' excited state, with calculated fractional $\ell > 0$ characters of 0.78 and 0.33 for detachment to the ground and excited states, respectively. As a result, the calculated cross section for photodetachment to the \tilde{X} state falls off more rapidly than for the \tilde{A} state, consistent with our ability to measure higher resolution SEVI spectra for the \tilde{A} band. Experimentally, these trends are supported by the results in Figures S6 and S7 of the [supplementary material](#) showing the attenuation of particular peaks as the eKE is decreased.

Anisotropy parameters for both electronic bands were found to be negative for the observed electron kinetic energies, in agreement with the results of Dyson orbital calculations (Figure S2 in the [supplementary material](#)). It should be noted that quantitative determination of the experimental PAD for the $\tilde{A}^2A' \leftarrow \tilde{X}^1A'$ electronic band was not feasible due to complications arising in reconstructing VMI images with high- eKE features that do not entirely fall on the phosphor screen. However, visual inspection of the VMI images indicates that the excited state band is more isotropic than the ground state band, which is another reflection of the finding that the $\tilde{A}^2A' \leftarrow \tilde{X}^1A'$ detachment transition yields photoelectrons with greater s -wave character than detachment to the neutral ground state.

VI. CONCLUSION

Cryo-SEVI spectra of $tBuOO^-$ are presented, providing well-resolved vibronic structure of the two lowest electronic states of the neutral radical. These spectra yield several vibrational frequencies for both electronic states of the neutral, which are assigned by comparison to Franck-Condon simulations. The high resolution of the cryo-SEVI experiment reveals low-frequency vibrational modes not reported in IR experiments and new vibrational structure that was not observed in the previously reported anion photoelectron spectrum of $tBuOO^-$. The refined electron affinity and vibrational frequencies reported in this work are benchmarks that will assist in future studies of reactions involving the $tBuOO$ radical and demonstrate the utility of cryo-SEVI as a spectroscopic probe for radical species.

SUPPLEMENTARY MATERIAL

See [supplementary material](#) for geometries, frequencies, calculated PADs, and descriptions of the geometry adjustments and partial wave analysis of Dyson orbitals described in the text.

ACKNOWLEDGMENTS

This research is funded by the Director, Office of Basic Energy Sciences, Chemical Sciences Division of the US Department of Energy under Contract No. DE-AC02-05CH11231. M.L.W. thanks the National Science Foundation for a graduate research fellowship.

- ¹S. W. Benson, *J. Am. Chem. Soc.* **87**, 972 (1964).
- ²P. D. Lightfoot, R. A. Cox, J. N. Crowley, M. Destriau, G. D. Hayman, M. E. Jenkin, G. K. Moortgat, and F. Zabel, *Atmos. Environ., Part A* **26**, 1805 (1992).
- ³T. J. Wallington, P. Dagaut, and M. J. Kurylo, *Chem. Rev.* **92**, 667 (1992).
- ⁴G. S. Tyndall, R. A. Cox, C. Granier, R. Lesclaux, G. K. Moortgat, M. J. Pilling, A. R. Ravishankara, and T. J. Wallington, *J. Geophys. Res.: Atmos.* **106**, 12157, doi:10.1029/2000jd900746 (2001).
- ⁵D. R. Glowacki and M. J. Pilling, *Chem. Phys. Chem.* **11**, 3836 (2010).
- ⁶F. Kirchner and W. R. Stockwell, *J. Geophys. Res.: Atmos.* **101**, 21007, doi:10.1029/96jd01519 (1996).
- ⁷B. J. Finlayson-Pitts and J. N. Pitts, *Science* **276**, 1045 (1997).
- ⁸J.-H. Xing and A. Miyoshi, *J. Phys. Chem. A* **109**, 4095 (2005).
- ⁹S. Goldstein and A. Samuni, *J. Phys. Chem. A* **111**, 1066 (2007).
- ¹⁰K. McKee, M. A. Blitz, and M. J. Pilling, *J. Phys. Chem. A* **120**, 1408 (2016).
- ¹¹J. R. Thomas, *J. Am. Chem. Soc.* **87**, 3935 (1965).
- ¹²A. Tomas and R. Lesclaux, *Chem. Phys. Lett.* **319**, 521 (2000).
- ¹³R. Lee, G. Grynova, K. U. Ingold, and M. L. Coote, *Phys. Chem. Chem. Phys.* **18**, 23676 (2016).
- ¹⁴M. S. Stark, *J. Am. Chem. Soc.* **122**, 4162 (2000).
- ¹⁵A. Tomas, E. Villenave, and R. Lesclaux, *Phys. Chem. Chem. Phys.* **2**, 1165 (2000).
- ¹⁶A. Miyoshi, *J. Phys. Chem. A* **115**, 3301 (2011).
- ¹⁷J. Zádor, C. A. Taatjes, and R. X. Fernandes, *Prog. Energy Combust. Sci.* **37**, 371 (2011).
- ¹⁸O. Welz, J. Zador, J. D. Savee, M. Y. Ng, G. Meloni, R. X. Fernandes, L. Sheps, B. A. Simmons, T. S. Lee, D. L. Osborn, and C. A. Taatjes, *Phys. Chem. Chem. Phys.* **14**, 3112 (2012).
- ¹⁹J. D. Savee, E. Papajak, B. Rotavera, H. Huang, A. J. Eskola, O. Welz, L. Sheps, C. A. Taatjes, and D. L. Osborn, *Science* **347**, 643 (2015).
- ²⁰H. E. Hunziker and H. R. Wendt, *J. Chem. Phys.* **64**, 3488 (1976).
- ²¹M. B. Pushkarsky, S. J. Zalyubovsky, and T. A. Miller, *J. Chem. Phys.* **112**, 10695 (2000).
- ²²E. N. Sharp, P. Rupper, and T. A. Miller, *Phys. Chem. Chem. Phys.* **10**, 3955 (2008).
- ²³P. Ase, W. Bock, and A. Snelson, *J. Phys. Chem.* **90**, 2099 (1986).
- ²⁴G. Meloni, P. Zou, S. J. Klippenstein, M. Ahmed, S. R. Leone, C. A. Taatjes, and D. L. Osborn, *J. Am. Chem. Soc.* **128**, 13559 (2006).
- ²⁵J. M. Oakes, L. B. Harding, and G. B. Ellison, *J. Chem. Phys.* **83**, 5400 (1985).
- ²⁶E. P. Clifford, P. G. Wenthold, R. Gareyev, W. C. Lineberger, C. H. DePuy, V. M. Bierbaum, and G. B. Ellison, *J. Chem. Phys.* **109**, 10293 (1998).
- ²⁷S. J. Blanksby, T. M. Ramond, G. E. Davico, M. R. Nimlos, S. Kato, V. M. Bierbaum, W. C. Lineberger, G. B. Ellison, and M. Okumura, *J. Am. Chem. Soc.* **123**, 9585 (2001).
- ²⁸M. Krauss and R. Osman, *J. Phys. Chem.* **99**, 11387 (1995).
- ²⁹J. L. Weisman and M. Head-Gordon, *J. Am. Chem. Soc.* **123**, 11686 (2001).
- ³⁰A. F. Gao, X. Sun, X. L. Liang, X. F. Fang, Z. Y. Zhu, and Y. P. Me, *J. Mol. Struct.: THEOCHEM* **862**, 105 (2008).
- ³¹W. Xu and G. Lu, *J. Phys. Chem. A* **112**, 6999 (2008).
- ³²J. Agarwal, A. C. Simmonett, and H. F. Schaefer, *Mol. Phys.* **110**, 2419 (2012).
- ³³D. A. Parkes and R. J. Donovan, *Chem. Phys. Lett.* **36**, 211 (1975).
- ³⁴G. Chettur and A. Snelson, *J. Phys. Chem.* **91**, 5873 (1987).
- ³⁵B. G. Glover and T. A. Miller, *J. Phys. Chem. A* **109**, 11191 (2005).

- ³⁶D. M. Neumark, *J. Phys. Chem. A* **112**, 13287 (2008).
- ³⁷E. P. Wigner, *Phys. Rev.* **73**, 1002 (1948).
- ³⁸A. Osterwalder, M. J. Nee, J. Zhou, and D. M. Neumark, *J. Chem. Phys.* **121**, 6317 (2004).
- ³⁹C. Hock, J. B. Kim, M. L. Weichman, T. I. Yacovitch, and D. M. Neumark, *J. Chem. Phys.* **137**, 244201 (2012).
- ⁴⁰M. L. Weichman, J. A. DeVine, D. S. Levine, J. B. Kim, and D. M. Neumark, *Proc. Natl. Acad. Sci. U. S. A.* **113**, 1698 (2016).
- ⁴¹U. Even, J. Jortner, D. Noy, N. Lavie, and C. Cossart-Magos, *J. Chem. Phys.* **112**, 8068 (2000).
- ⁴²J. B. Kim, C. Hock, T. I. Yacovitch, and D. M. Neumark, *J. Phys. Chem. A* **117**, 8126 (2013).
- ⁴³W. C. Wiley and I. H. McLaren, *Rev. Sci. Instrum.* **26**, 1150 (1955).
- ⁴⁴A. T. J. B. Eppink and D. H. Parker, *Rev. Sci. Instrum.* **68**, 3477 (1997).
- ⁴⁵D. W. Chandler and P. L. Houston, *J. Chem. Phys.* **87**, 1445 (1987).
- ⁴⁶M. B. Doyle, C. Abeyasera, and A. G. Suits, NuACQ, <http://faculty.missouri.edu/suitsa/NuAqc.html>.
- ⁴⁷B. Dick, *Phys. Chem. Chem. Phys.* **16**, 570 (2014).
- ⁴⁸C. Blondel, W. Chaibi, C. Delsart, C. Drag, F. Goldfarb, and S. Kroger, *Eur. Phys. J. D* **33**, 335 (2005).
- ⁴⁹C. Blondel, W. Chaibi, C. Delsart, and C. Drag, *J. Phys. B: At., Mol. Opt. Phys.* **39**, 1409 (2006).
- ⁵⁰J. Cooper and R. N. Zare, *J. Chem. Phys.* **48**, 942 (1968).
- ⁵¹K. J. Reed, A. H. Zimmerman, H. C. Andersen, and J. I. Brauman, *J. Chem. Phys.* **64**, 1368 (1975).
- ⁵²A. Sanov, *Annu. Rev. Phys. Chem.* **65**, 341 (2014).
- ⁵³Y. Shao, Z. Gan, E. Epifanovsky, A. T. B. Gilbert, M. Wormit, J. Kussmann, A. W. Lange, A. Behn, J. Deng, X. Feng, D. Ghosh, M. Goldey, P. R. Horn, L. D. Jacobson, I. Kaliman, R. Z. Khaliullin, T. K us, A. Landau, J. Liu, E. I. Proynov, Y. M. Rhee, R. M. Richard, M. A. Rohrdanz, R. P. Steele, E. J. Sundstrom, H. L. Woodcock III, P. M. Zimmerman, D. Zuev, B. Albrecht, E. Alguire, B. Austin, G. J. O. Beran, Y. A. Bernard, E. Berquist, K. Brandhorst, K. B. Bravaya, S. T. Brown, D. Casanova, C.-M. Chang, Y. Chen, S. H. Chien, K. D. Closser, D. L. Crittenden, M. Diedenhofen, R. A. DiStasio, Jr., H. Dop, A. D. Dutoi, R. G. Edgar, S. Fatehi, L. Fusti-Molnar, A. Ghysels, A. Golubeva-Zadorozhnaya, J. Gomes, M. W. D. Hanson-Heine, P. H. P. Harbach, A. W. Hauser, E. G. Hohenstein, Z. C. Holden, T.-C. Jagau, H. Ji, B. Kaduk, K. Khistyayev, J. Kim, J. Kim, R. A. King, P. Klunzinger, D. Kosenkov, T. Kowalczyk, C. M. Krauter, K. U. Lao, A. Laurent, K. V. Lawler, S. V. Levchenko, C. Y. Lin, F. Liu, E. Livshits, R. C. Lochan, A. Luenser, P. Manohar, S. F. Manzer, S.-P. Mao, N. Mardirossian, A. V. Marenich, S. A. Maurer, N. J. Mayhall, C. M. Oana, R. Olivares-Amaya, D. P. O'Neill, J. A. Parkhill, T. M. Perrine, R. Peverati, P. A. Pieniazek, A. Prociuk, D. R. Rehn, E. Rosta, N. J. Russ, N. Sergueev, S. M. Sharada, S. Sharma, D. W. Small, A. Sodt, T. Stein, D. St uck, Y.-C. Su, A. J. W. Thom, T. Tsuchimochi, L. Vogt, O. Vydrov, T. Wang, M. A. Watson, J. Wenzel, A. White, C. F. Williams, V. Vanovschi, S. Yeganeh, S. R. Yost, Z.-Q. You, I. Y. Zhang, X. Zhang, Y. Zhou, B. R. Brooks, G. K. L. Chan, D. M. Chipman, C. J. Cramer, W. A. Goddard III, M. S. Gordon, W. J. Hehre, A. Klamt, H. F. Schaefer III, M. W. Schmidt, C. D. Sherrill, D. G. Truhlar, A. Warshel, X. Xua, A. Aspuru-Guzik, R. Baer, A. T. Bell, N. A. Besley, J.-D. Chai, A. Dreuw, B. D. Dunietz, T. R. Furlani, S. R. Gwaltney, C.-P. Hsu, Y. Jung, J. Kong, D. S. Lambrecht, W. Liang, C. Ochsenfeld, V. A. Rassolov, L. V. Slipchenko, J. E. Subotnik, T. Van Voorhis, J. M. Herbert, A. I. Krylov, P. M. W. Gill, and M. Head-Gordon, *Mol. Phys.* **113**, 184 (2015).
- ⁵⁴A. I. Krylov and P. M. W. Gill, *Wiley Interdiscip. Rev.: Comput. Mol. Sci.* **3**, 317 (2013).
- ⁵⁵J. B. Kim, M. L. Weichman, T. I. Yacovitch, C. Shih, and D. M. Neumark, *J. Chem. Phys.* **139**, 104301 (2013).
- ⁵⁶M. L. Weichman, J. B. Kim, and D. M. Neumark, *J. Phys. Chem. A* **119**, 6140 (2015).
- ⁵⁷J. A. DeVine, M. L. Weichman, S. J. Lyle, and D. M. Neumark, *J. Mol. Spectrosc.* **332**, 16 (2017).
- ⁵⁸A. T. B. Gilbert, N. A. Besley, and P. M. W. Gill, *J. Phys. Chem. A* **112**, 13164 (2008).
- ⁵⁹S. Gozem and A. I. Krylov, ezDyson 3.2, iOpenShell Center for Computational Studies of Electronic Structure and Spectroscopy of Open-Shell and Electronically Excited Species, Los Angeles, <http://iopenshell.usc.edu/downloads>.
- ⁶⁰C. M. Oana and A. I. Krylov, *J. Chem. Phys.* **131**, 124114 (2009).
- ⁶¹V. A. Mozhayskiy and A. I. Krylov, ezSpectrum 3.0, iOpenShell Center for Computational Studies of Electronic Structure and Spectroscopy of Open-Shell and Electronically Excited Species, Los Angeles, <http://iopenshell.usc.edu/downloads>.